



Cite as
Nano-Micro Lett.
(2023) 15:118

Received: 2 February 2023
Accepted: 21 March 2023
Published online: 30 April 2023
© The Author(s) 2023

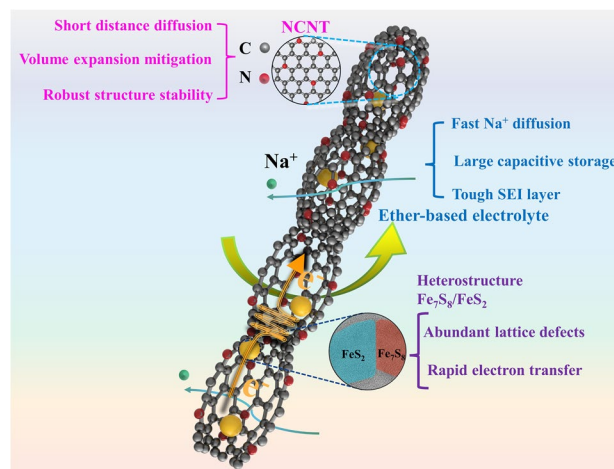
Interface Engineering of Fe₇S₈/FeS₂ Heterostructure in situ Encapsulated into Nitrogen-Doped Carbon Nanotubes for High Power Sodium-Ion Batteries

Penghao Song¹, Jian Yang^{1,3}, Chengyin Wang¹, Tianyi Wang¹ ✉, Hong Gao² ✉, Guoxiu Wang² ✉, Jiabao Li¹ ✉

HIGHLIGHTS

- Iron sulfide-based heterostructure in situ hybridized with nitrogen-doped carbon nanotubes was prepared through a successive pyrolysis and sulfidation approach.
- The as-prepared Fe₇S₈/FeS₂/NCNT electrode exhibits superior sodium storage performance in both ester and ether-based electrolytes.
- The structure advantages of the electrode contribute to high electrochemical performance in the ester-based electrolyte, while fast ionic diffusion and favorable capacitive behavior result in the robust sodium storage performance in the ether-based electrolyte.

ABSTRACT Heterostructure engineering combined with carbonaceous materials shows great promise toward promoting sluggish kinetics, improving electronic conductivity, and mitigating the huge expansion of transition metal sulfide electrodes for high-performance sodium storage. Herein, the iron sulfide-based heterostructures in situ hybridized with nitrogen-doped carbon nanotubes (Fe₇S₈/FeS₂/NCNT) have been prepared through a successive pyrolysis and sulfidation approach. The Fe₇S₈/FeS₂/NCNT heterostructure delivered a high reversible capacity of 403.2 mAh g⁻¹ up to 100 cycles at 1.0 A g⁻¹ and superior rate capability (273.4 mAh g⁻¹ at 20.0 A g⁻¹) in ester-based electrolyte. Meanwhile, the electrodes also demonstrated long-term cycling stability (466.7 mAh g⁻¹ after 1,000 cycles at 5.0 A g⁻¹) and outstanding rate capability (536.5 mAh g⁻¹ at 20.0 A g⁻¹) in ether-based electrolyte. This outstanding performance could be mainly attributed to the fast sodium-ion diffusion kinetics, high capacitive contribution, and convenient interfacial dynamics in ether-based electrolyte.



KEYWORDS Iron sulfides; Heterostructure; Nitrogen-doped carbon nanotubes; Ester-based electrolyte; Ether-based electrolyte

✉ Tianyi Wang, wangty@yzu.edu.cn; Hong Gao, hong.gao@uts.edu.au; Guoxiu Wang, guoxiu.wang@uts.edu.au; Jiabao Li, jiabaoli@yzu.edu.cn

¹ College of Chemistry and Chemical Engineering, Yangzhou University, 180 Si-Wang-Ting Road, Yangzhou 225002, Jiangsu, People's Republic of China

² Centre for Clean Energy Technology, Faculty of Science, University of Technology Sydney, PO Box 123, Broadway, NSW 2007, Australia

³ Key Lab of Fluorine and Silicon for Energy Materials and Chemistry of Ministry of Education, College of Chemistry and Chemical Engineering, Jiangxi Normal University, Nanchang 330022, People's Republic of China



1 Introduction

Sodium-ion batteries (SIBs) with a similar operating mechanism to lithium-ion batteries and abundant sodium resources are considered as one of the most promising candidates for low-cost renewable energy storage [1–5]. However, sodium ion has a relatively large ionic radius and sluggish reaction kinetics, which inevitably lead to capacity degradation and cycling instability, hindering the practical application of SIBs [6–10]. Therefore, it is of great significance to develop novel electrode materials with high capacity and long cycle life.

Transition metal sulfides (TMSs) are considered as promising electrode candidates due to their high theoretical capacities [11–15]. The weak M-S bond is favorable for electrochemical conversion reaction, resulting in active redox kinetics and reversibility. As a typical TMSs, pyrite FeS_2 with a high theoretical capacity (894 mAh g^{-1}), low cost, and environmental friendliness, is a promising and effective sodium storage electrode material [16–19]. However, similar to other metal sulfides, the iron sulfides-based electrodes suffer from poor electronic conductivity and huge volume change upon cycling, resulting in sluggish Na^+ insertion/extraction, large electrochemical polarization, electrode degradation, and hence poor rate capability and limited cycling life [20–23].

To overcome the above mentioned challenges, many efforts have been made, mainly focusing on several aspects [24–27]. These include: (i) Combining with conductive matrix to accelerate electron transport and alleviate the structure expansion of the active material during cycling; (ii) Creating a large number of lattice defects to provide abundant active sites; (iii) Optimizing the electrolyte to facilitate Na^+ diffusion kinetics, improve the capacitive contribution of charge storage, and form robust solid electrolyte interface- (SEI) layer. Liu et al. [28] designed FeS_2 nanocrystals wrapped in a turbostratic carbon framework ($\text{FeS}_2\text{-C}$) via a mechanical alloying process. The $\text{FeS}_2\text{-C}$ electrode achieved rapid electrons/ions transport and robust structural stability, thus enabling improved rate capability and long cycling performance for SIBs. Chen et al. [29] designed $\text{Fe}_{1-x}\text{S}/\text{MoS}_2$ heterostructure with abundant active sites, and the corresponding electrode exhibited good rate capability and stable cycling performance. In addition to improving the sodium storage performance from the perspective of material

synthesis, it was also found that different electrolytes can greatly affect the structural transformation and electrochemical performance of FeS_2 -based anodes during cycling. Zhou et al. [30] demonstrated that the $\text{FeS}_2\text{@C}$ electrode coupled with ether-based electrolyte could realize high ionic diffusion and electrochemical reversibility. These individual modification strategies can indeed modify the performance of iron chalcogenide-based electrodes. Therefore, the combination of the above three strategies will simultaneously endow the electrodes with high conductivity, rapid charge transfer, and favorable interfacial behaviors.

Herein, we rationally designed and prepared iron sulfide-based heterostructures encapsulated in N-doped carbon nanotubes ($\text{Fe}_7\text{S}_8/\text{FeS}_2/\text{NCNT}$) via an in situ pyrolysis and sulfidation strategy. The as-prepared $\text{Fe}_7\text{S}_8/\text{FeS}_2/\text{NCNT}$ heterostructures inherit substantial lattice defects and sufficient buffer space offered by the NCNT, which endow the $\text{Fe}_7\text{S}_8/\text{FeS}_2/\text{NCNT}$ electrode with high sodium storage activity, rapid ionic diffusion kinetics, and excellent electrochemical reversibility. Interestingly, the electrochemical performance of $\text{Fe}_7\text{S}_8/\text{FeS}_2/\text{NCNT}$ electrode can be further improved in ether-based electrolyte. We also systematically investigated the ion diffusion kinetics, charge storage mechanism, and SEI composition of the $\text{Fe}_7\text{S}_8/\text{FeS}_2/\text{NCNT}$ electrodes in different electrolytes.

2 Experimental Section

2.1 Preparation of Fe/NCNT

A facile pyrolysis method was applied to prepare the Fe/NCNT precursor. Typically, 10 mL of deionized water and 250 mg dicyandiamide (DICY) were mixed together under stirring, and then 50 mg ferric chloride (FeCl_3) was added into the above aqueous solution and stirred for 1 h at room temperature. The mixture was then dried in 80°C water bath to obtain light red powder (DICY-Fe). After that, the product was ground and calcined at 800°C for 2 h under argon to receive the desired Fe/NCNT.

2.2 Preparation of $\text{Fe}_7\text{S}_8/\text{FeS}_2/\text{NCNT}$

The obtained Fe/NCNT and sulfur powder with a mass ratio of 1:3 were placed in an alumina boat, then annealed

at 600 °C (heating rate of 2 °C min⁻¹) for 2 h under argon atmosphere to get the Fe₇S₈/NCNT. Then the Fe₇S₈/NCNT and sulfur powder with a mass ratio of 1:1 were calcinated at 400 °C (heating rate of 2 °C min⁻¹) for 1 h under argon to obtain the Fe₇S₈/FeS₂/NCNT. For comparison, the Fe₇S₈/NCNT and sulfur powder with a mass ratio of 1:3 were calcinated at 400 °C for 4 h under argon to obtain the FeS₂/NCNT.

The detailed material characterizations and electrochemical measurements were provided in the Supporting Information.

3 Results and Discussion

3.1 Physical Characterization Results

The fabrication strategy of Fe₇S₈/FeS₂/NCNT is illustrated in Fig. 1a. Firstly, based on the coordination of the cyanogen groups in dicyandiamide (DICY) with the Fe³⁺, the unique DICY-Fe precursors can be obtained. Interestingly, owing to the high catalytic effect of iron species in the precursor,

the nitrogen-doped carbon nanotubes can be formed during the subsequent carbonization process, resulting in the Fe/NCNT composite [31]. The subsequent sulfidation procedure in situ converts the Fe/NCNT into Fe₇S₈/FeS₂ heterostructures coated by NCNT. The Fe₇S₈/FeS₂ heterostructures can induce a large number of lattice defects and rapid charge transfer, which together with the excellent electronic conductivity and sufficient buffer space offered by the NCNT, contribute to boosting the electrochemical sodium storage performance [32, 33].

Scanning electron microscopy (SEM) and transmission electron microscopy (TEM) were employed to investigate the morphology features of the as-prepared samples. The SEM image of Fe/NCNT (Fig. S1a) reveals regular nanotube morphology with diameters of about tens of nanometers, indicating the conversion from the DICY-Fe complexes to Fe species confined into the carbon nanotubes after carbonization. The SEM images of Fe₇S₈/NCNT, FeS₂/NCNT, and Fe₇S₈/FeS₂/NCNT are shown in Figs. S1b, c and 1b, respectively. Their morphologies are not very different, and the nanotube morphologies are well maintained, indicating that

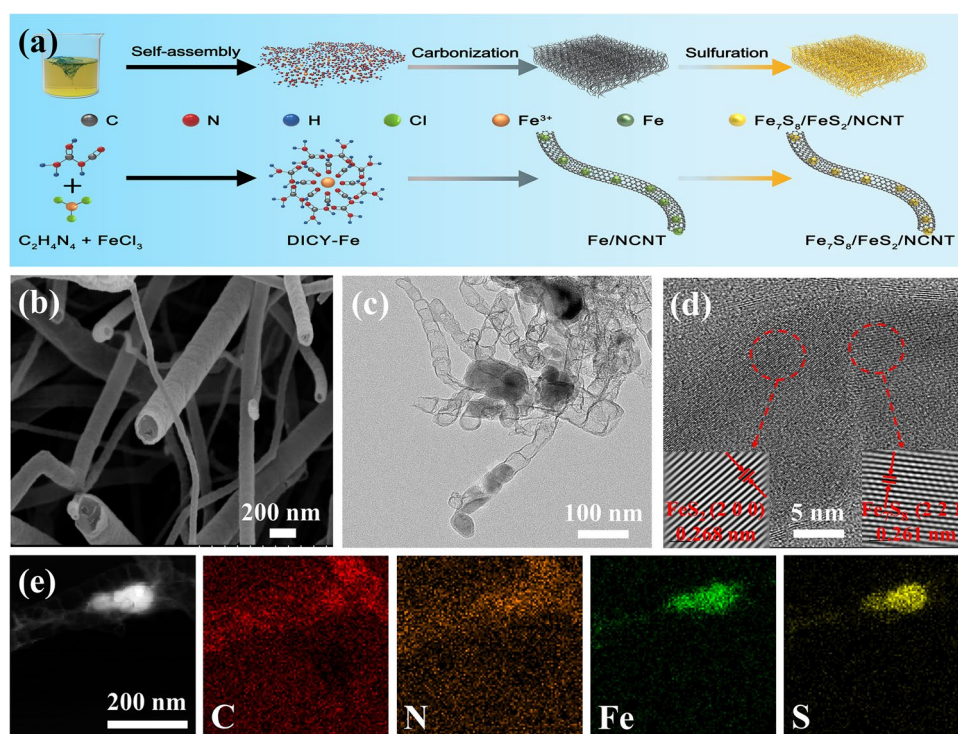


Fig. 1 (a) Schematic illustration of the preparation, (b) SEM image, (c) TEM image, (d) HRTEM image, (e) STEM and corresponding elemental mapping images of Fe₇S₈/FeS₂/NCNT

the sulfidation treatment has little effect on their morphologies. The carbon nanotube possesses a highly conductive network to accelerate the charge transfer, the large specific surface area provides efficient buffer matrix, and the large internal space can accommodate volume expansion during repeated charging/discharging processes, all of which contribute to high sodium storage performance [34, 35]. Furthermore, TEM images of $\text{Fe}_7\text{S}_8/\text{FeS}_2/\text{NCNT}$ (Fig. 1c) demonstrate that the $\text{Fe}_7\text{S}_8/\text{FeS}_2$ was embedded in the hollow carbon nanotube, which would be beneficial to alleviate the volume expansion of the $\text{Fe}_7\text{S}_8/\text{FeS}_2/\text{NCNT}$ heterostructure during electrochemical cycling process, thus maintaining the integrity of the electrode [34]. More structure information of the $\text{Fe}_7\text{S}_8/\text{FeS}_2/\text{NCNT}$ was obtained through the high-resolution transmission electron microscopy (HRTEM), where the lattice fringes with d-spacings of 0.261 and 0.268 nm correspond to (2 2 1) plane of Fe_7S_8 and (2 0 0) planes of FeS_2 , respectively, can be detected (Fig. 1d) [36, 37]. And lattice peak position period diagrams (Fig. S2) further prove the reliability of lattice spacings of Fe_7S_8 and FeS_2 . Moreover, the heterointerface between the Fe_7S_8 and FeS_2 can be clearly observed, further indicating the successful

synthesis of the heterostructures, which contribute to rapid charge transfer [33, 38]. Besides, the selected area electron diffraction (SAED) pattern of $\text{Fe}_7\text{S}_8/\text{FeS}_2/\text{NCNT}$ (Fig. S3) manifests that the clear diffraction rings can be well indexed to the (4 1 1), and (2 2 0) planes of cubic FeS_2 and (-2 2 1) and (-6 2 3) planes of monoclinic Fe_7S_8 [36, 37]. The STEM and related elemental mappings of $\text{Fe}_7\text{S}_8/\text{FeS}_2/\text{NCNT}$ are displayed in Fig. 1e. Clearly, C and N elements are uniformly distributed throughout the structure, while Fe and S are concentrated in the lumen of the nanotube, further showing the confined structure [38]. The intercalation design of heterostructure in NCNTs can significantly alleviate the structure expansion/contraction of the electrode and effectively improve the electronic conductivity of the composite [38].

To preliminarily determine the phase structures of as-prepared samples, X-ray powder diffraction (XRD) measurements were performed. Particularly, the diffraction peaks of the as-synthesized Fe/NCNT (Fig. S4) can be well indexed to the cubic Fe (JCPDS No. 03-1050), indicating the successful conversion from the DIC-Fe to Fe/NCNT [39]. In Fig. 2a, the XRD pattern of $\text{Fe}_7\text{S}_8/\text{FeS}_2/\text{NCNT}$ manifests

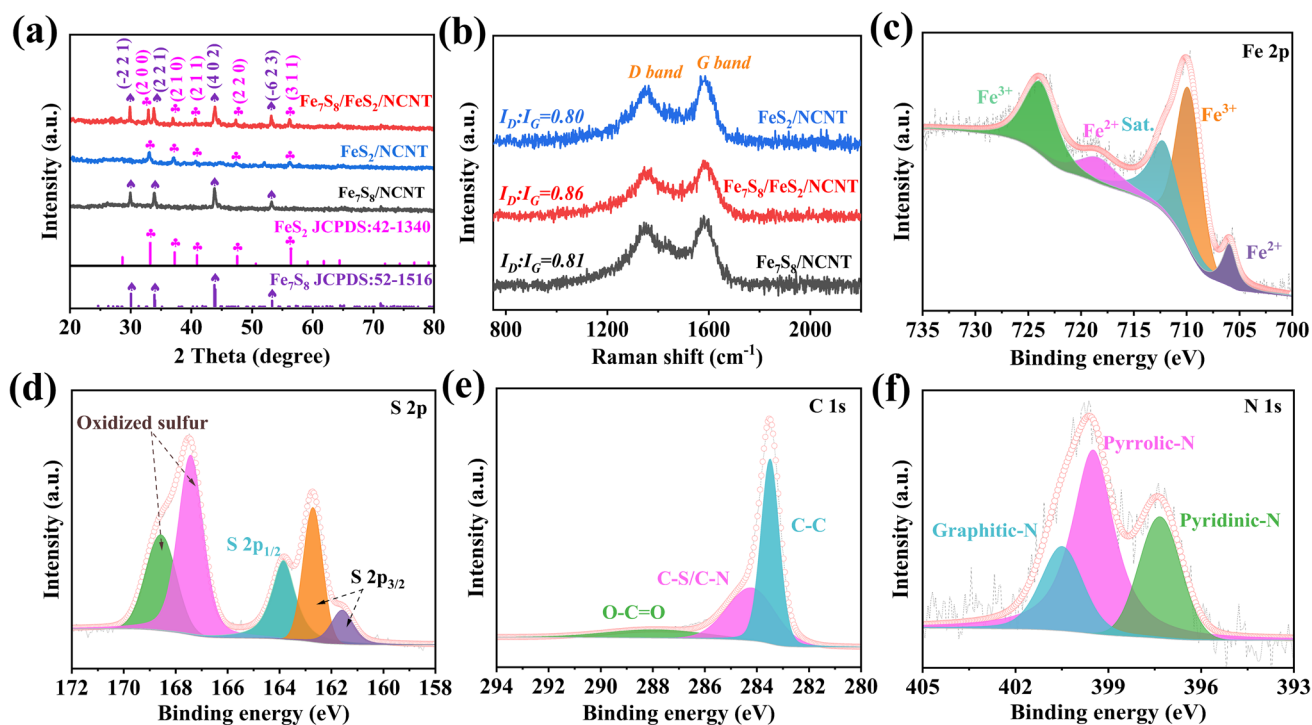


Fig. 2 (a) XRD patterns and (b) Raman spectra of the $\text{Fe}_7\text{S}_8/\text{NCNT}$, FeS_2/NCNT , and $\text{Fe}_7\text{S}_8/\text{FeS}_2/\text{NCNT}$. XPS spectra of the $\text{Fe}_7\text{S}_8/\text{FeS}_2/\text{NCNT}$: (c) Fe 2p, (d) S 2p, (e) C 1s and (f) N 1s

the characteristic peaks of monoclinic Fe_7S_8 (JCPDS No. 52–1516) and cubic FeS_2 (JCPDS No. 42–1340) [40, 41]. Specifically, the diffraction peaks located at around 29.9° , 33.8° , 43.7° , and 53.2° correspond to the $(-2\ 1\ 1)$, $(2\ 2\ 1)$, $(4\ 0\ 2)$, and $(-6\ 2\ 3)$ planes of monoclinic Fe_7S_8 , while the diffraction peaks centered at around 33.1° , 37.1° , 40.7° , 47.4° and 56.3° can be ascribed to the $(2\ 0\ 0)$, $(2\ 1\ 0)$, $(2\ 1\ 1)$, $(2\ 2\ 0)$ and $(3\ 1\ 1)$ planes of cubic FeS_2 , respectively, thereby indicating the successful fabrication of the target heterostructure [40, 41]. For comparison, the XRD patterns of $\text{Fe}_7\text{S}_8/\text{NCNT}$ and FeS_2/NCNT can be identified with monoclinic Fe_7S_8 and cubic FeS_2 , respectively. While no diffraction peak related to the NCNT can be observed, mainly due to their amorphous state and low content. To confirm the existence of NCNT, Raman spectra are performed (Fig. 2b). Apparently, two broad peaks can be detected at around 1588 and $1351\ \text{cm}^{-1}$, which is attributed to the graphitic structure (G bands) and disordered domain (D bands) in the carbonaceous skeleton, respectively [27]. Particularly, the higher I_D/I_G value of $\text{Fe}_7\text{S}_8/\text{FeS}_2/\text{NCNT}$ (0.86) than those of $\text{Fe}_7\text{S}_8/\text{NCNT}$ (0.81) and FeS_2/NCNT (0.80) means that the more defects generated in the heterostructure, offering extra active sites and contributing to improving the sodium storage performance [29]. Meanwhile, the NCNT content of $\text{Fe}_7\text{S}_8/\text{FeS}_2/\text{NCNT}$ is characterized by thermogravimetric (TG) analysis. As shown in Fig. S5, the weight loss is attributed to the oxidation of $\text{Fe}_7\text{S}_8/\text{FeS}_2$ and N-doped carbon in air. Based on the fact that the sulfidation process will not change the mass ratio of Fe element to NCNT from Fe/NCNT to $\text{Fe}_7\text{S}_8/\text{FeS}_2/\text{NCNT}$, thus the content of NCNT in $\text{Fe}_7\text{S}_8/\text{FeS}_2/\text{NCNT}$ is calculated to be 30.4% [16].

Furthermore, the surface component and elemental oxidation state of the obtained $\text{Fe}_7\text{S}_8/\text{NCNT}$, $\text{Fe}_7\text{S}_8/\text{FeS}_2/\text{NCNT}$, and FeS_2/NCNT samples were characterized through X-ray photoelectron spectroscopy (XPS). The XPS survey spectra of all samples shown in Fig. S6 verify the co-existence of elements Fe, S, C, and N in the target samples. Note that the appearance of O 1s peak should be ascribed to the exposure to air [18]. As shown in Fig. 2c, the Fe 2p spectrum of $\text{Fe}_7\text{S}_8/\text{FeS}_2/\text{NCNT}$ exhibits two peaks at 706.2 and 718.6 eV, respectively, which confirms the existence of Fe^{2+} , and the characteristic signals for Fe^{3+} can be observed at around 710.6 and 724.6 eV [19]. For the S 2p spectrum shown in Fig. 2d, the S 2p_{3/2} species can be detected at around 161.6 and 162.7 eV. In addition, the presence of S 2p_{1/2} can be confirmed by the peak detected at 163.8 eV, and two peaks

at around 167.5 and 168.6 eV correspond to oxidized sulfur, which may be attributed to the oxidization of metal sulfides in air [27]. Regarding the N 1s spectrum (Fig. 2e), three peaks located at around 397.3 (pyridinic-N), 399.5 (pyrrolic-N), and 400.5 (graphitic-N) eV, respectively, can be detected [42]. In regard to the C 1s spectrum (Fig. 2f), a dominant peak at around 283.5 eV can be indexed to the C–C, while another two weak peaks at 284.0 and 288.1 eV can be ascribed to the C–N/C–S and O–C=O, respectively [43]. For comparison, the XPS spectra of the $\text{Fe}_7\text{S}_8/\text{NCNT}$ and FeS_2/NCNT were also investigated, as shown in Figs. S7 and S8. Both the N 1s and C 1s spectra of the $\text{Fe}_7\text{S}_8/\text{NCNT}$ and FeS_2/NCNT composites are almost identical to those of $\text{Fe}_7\text{S}_8/\text{FeS}_2/\text{NCNT}$. Apparently, the Fe 2p and S 2p spectra of $\text{Fe}_7\text{S}_8/\text{NCNT}$ and FeS_2/NCNT show distinct differences, revealing different valence states of Fe and S in the two samples. Notably, the obvious oxidized sulfur peak in the S 2p spectrum of FeS_2/NCNT should be ascribed to the surface oxidization upon sulfidation [27].

3.2 Electrochemical Results

The sodium storage performances of as-prepared samples were investigated in ester-based electrolyte. The comparison of initial cyclic voltammetry (CV) curves of $\text{Fe}_7\text{S}_8/\text{NCNT}$, $\text{Fe}_7\text{S}_8/\text{FeS}_2/\text{NCNT}$, and FeS_2/NCNT electrodes are shown in Fig. 3a. Compared with the initial CV curves of $\text{Fe}_7\text{S}_8/\text{NCNT}$ and FeS_2/NCNT electrodes, the $\text{Fe}_7\text{S}_8/\text{FeS}_2/\text{NCNT}$ exhibits reduction peaks at 0.97 and 0.61 V, which can be assigned to the Na^+ insertion into cubic FeS_2 and monoclinic Fe_7S_8 , respectively [18]. Subsequently, the reduction peak at 0.18 V can be indexed to the conversion from $\text{Fe}^{2+}/\text{Fe}^{3+}$ to Fe^0 [18]. As for the subsequent anodic scan, the formation of Na_xFeS_2 can be confirmed through the peak at around 1.42 V, while another two peaks at around 1.85 and 2.54 V can be ascribed to the desodiation of Na_xFeS_2 [37, 41]. To detect the detailed electrochemical behaviors of the obtained $\text{Fe}_7\text{S}_8/\text{FeS}_2/\text{NCNT}$, the initial four CV curves at $0.2\ \text{mV s}^{-1}$ have been depicted in Fig. S9a. The irreversible phase transition at the first cathodic scan can be attributed to the passivation process of the electrode surface, accompanied by the decomposition of electrolyte and the generation of SEI [44]. Afterward, the substantially overlapping CV curves of the $\text{Fe}_7\text{S}_8/\text{FeS}_2/\text{NCNT}$ indicate its excellent electrochemical reversibility and structural stability [44]. In contrast, the

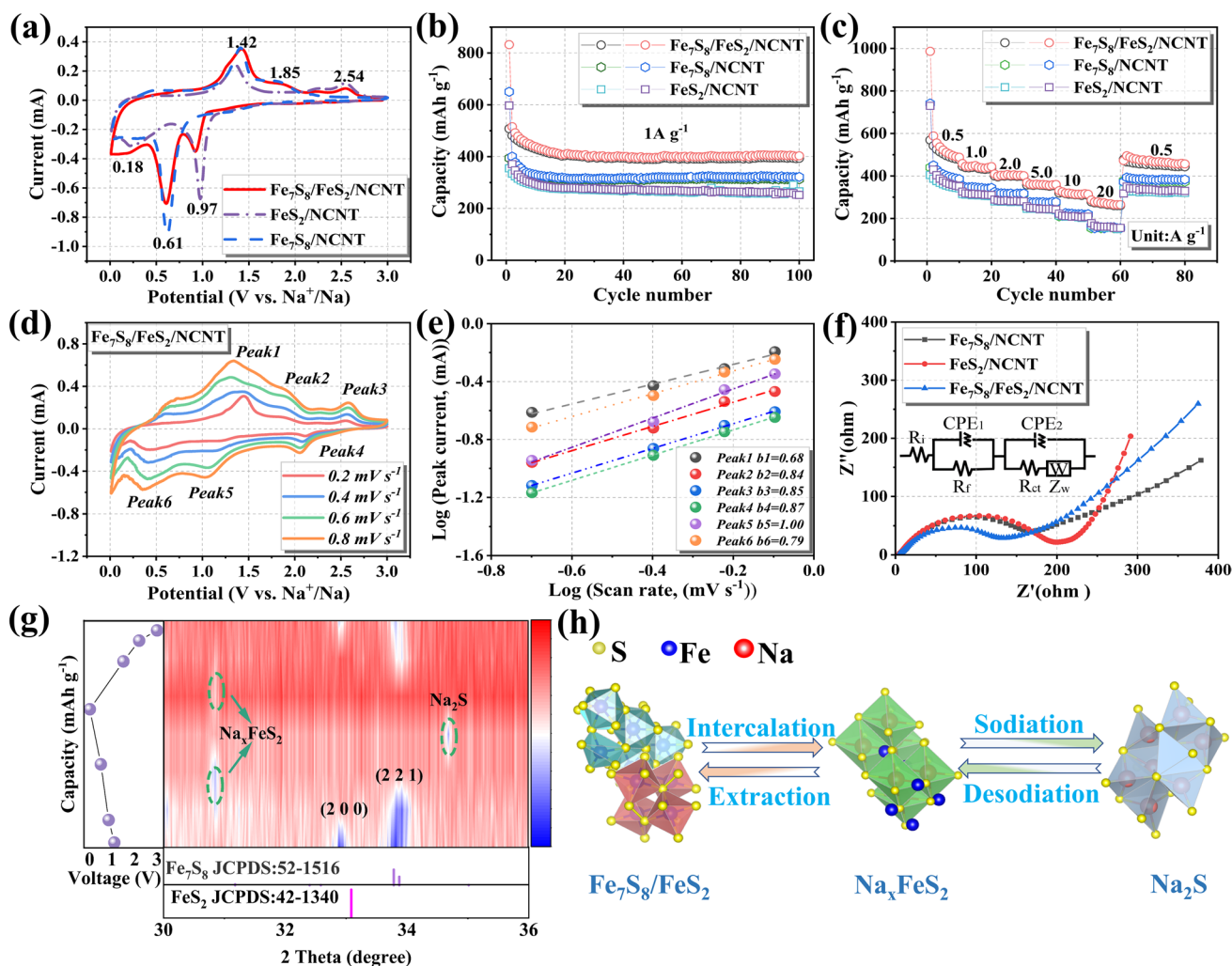


Fig. 3 (a) Comparison of the first CV curves at 0.2 mV s^{-1} , (b) cycling performances, and (c) rate capabilities of $\text{Fe}_7\text{S}_8/\text{NCNT}$, FeS_2/NCNT , and $\text{Fe}_7\text{S}_8/\text{FeS}_2/\text{NCNT}$ electrodes. (d) CV curves at different scan rates (from 0.2 to 0.8 mV s^{-1}) and (e) linear relationship of peak currents $\text{Log}(i)$ versus scan rate $\text{Log}(v)$ of the $\text{Fe}_7\text{S}_8/\text{FeS}_2/\text{NCNT}$ electrode. (f) Nyquist plots of the $\text{Fe}_7\text{S}_8/\text{NCNT}$, FeS_2/NCNT , and $\text{Fe}_7\text{S}_8/\text{FeS}_2/\text{NCNT}$ electrodes after 50 cycles at 1.0 A g^{-1} . (g) XRD contour map at different charging/discharging states, and (h) reaction mechanism illustration during sodiation and desodiation process of the $\text{Fe}_7\text{S}_8/\text{FeS}_2/\text{NCNT}$ electrode

$\text{Fe}_7\text{S}_8/\text{NCNT}$ and FeS_2/NCNT electrodes show reduced electrochemical reversibility, which can be detected from Fig. S9b, c. Accordingly, the voltage plateaus in the charge/discharge voltage curves of $\text{Fe}_7\text{S}_8/\text{FeS}_2/\text{NCNT}$, $\text{Fe}_7\text{S}_8/\text{NCNT}$, and FeS_2/NCNT electrodes are highly consistent with the redox peaks presented in the CV results (Fig. S9d–f).

To further highlight the structural advantage of the $\text{Fe}_7\text{S}_8/\text{FeS}_2/\text{NCNT}$ as anode material for SIBs, the comparison of cycling stability of the as-fabricated electrodes was conducted (Fig. 3b). The $\text{Fe}_7\text{S}_8/\text{FeS}_2/\text{NCNT}$, $\text{Fe}_7\text{S}_8/\text{NCNT}$, and FeS_2/NCNT electrodes deliver reversible capacities of 403.2 , 321.7 and 252.1 mAh g^{-1} , respectively, at 1.0 A g^{-1}

after 100 cycles, indicating the excellent electrochemical activity of the designed heterostructure. In regard to the rate capability, the $\text{Fe}_7\text{S}_8/\text{FeS}_2/\text{NCNT}$ electrode can deliver average reversible capacities of 521.9 (0.5 A g^{-1}), 448.5 (1.0 A g^{-1}), 406.6 (2.0 A g^{-1}), 359.7 (5.0 A g^{-1}) and 316.7 (10.0 A g^{-1}) mAh g^{-1} , respectively (Fig. 3c). Surprisingly, a satisfied reversible capacity of 273.4 mAh g^{-1} can still be achieved even at a high current density of 20.0 A g^{-1} , which means that the battery can be fully charged and discharged within 1 min. In contrast, the $\text{Fe}_7\text{S}_8/\text{NCNT}$ and FeS_2/NCNT electrodes can only deliver reversible capacities of 153.8 and 161.1 mAh g^{-1} at 20.0 A g^{-1} , respectively. Besides,

the charge–discharge rate profiles of the $\text{Fe}_7\text{S}_8/\text{FeS}_2/\text{NCNT}$ electrode reveal that the voltage plateaus of the curves at different current densities can be well maintained (Fig. S10a). For the $\text{Fe}_7\text{S}_8/\text{NCNT}$ and FeS_2/NCNT electrodes, the gradually degraded plateaus and decreased capacities suggest their poor structure stability (Fig. S10b, c) [45].

In order to reveal the kinetics origin and reaction mechanism of the target $\text{Fe}_7\text{S}_8/\text{FeS}_2/\text{NCNT}$ electrode, CV curves collected from 0.2 to 0.8 mV s^{-1} scan rates have been performed (Fig. 3d). Compared with the CV curves of $\text{Fe}_7\text{S}_8/\text{NCNT}$ and FeS_2/NCNT electrode (Fig. S11), the CV shape of $\text{Fe}_7\text{S}_8/\text{FeS}_2/\text{NCNT}$ is well-maintained with increasing scan rate, indicating its weak electrochemical polarization and excellent electrochemical reversibility. It is well known that both diffusion and capacitive behaviors contribute to the charge stored in electrode, and the response current and scan rate obey the following equation [12, 45]:

$$i = a v^b \quad (1)$$

where a is a variable parameter, and the value of b is a typical index to judge the reaction kinetics, and it can be received from the slope after plotting $\log(i)$ versus $\log(v)$. Generally, the value of b close to 1.0 corresponds to a pseudocapacitive process, while the value approaching to 0.5 means that the electrochemical process is dominated by diffusion [46]. In Fig. 3e, the b values after fitting for the oxidation peaks are 0.68 (peak 1), 0.84 (peak 2), and 0.85 (peak 3), and the corresponding values of the reduction peaks are 0.87 (peak 4), 1.00 (peak 5) and 0.79 (peak 6), indicating that the charge stored in the $\text{Fe}_7\text{S}_8/\text{FeS}_2/\text{NCNT}$ electrode is dominated by both diffusion and capacitive behaviors [13, 32]. Generally, the mixed charge storage mechanism can not only provide high reaction kinetics through the pseudocapacitive behavior, but also induce high utilization of the active material, thus guaranteeing high electrochemical sodium storage performance [32]. In addition, the Nyquist plots of the three electrodes after 50 cycles at 1.0 A g^{-1} manifest that the $\text{Fe}_7\text{S}_8/\text{FeS}_2/\text{NCNT}$ electrode displays a lower charge transfer resistance (93.5 Ω) compared with those of $\text{Fe}_7\text{S}_8/\text{NCNT}$ (130.1 Ω) and FeS_2/NCNT (134.4 Ω), indicating better electrochemical kinetics of the special designed $\text{Fe}_7\text{S}_8/\text{FeS}_2/\text{NCNT}$ heterostructure (Fig. 3f) [21, 23]. Therefore, the high capacitive contribution of the charge storage as well as the low energy barrier of charge transfer can facilitate the electrons/ions transport, thus dramatically decreasing the electrochemical polarization.

Furthermore, in order to reveal the working mechanism of the $\text{Fe}_7\text{S}_8/\text{FeS}_2/\text{NCNT}$ electrode, ex situ XRD measurements for the target electrode at selected voltages upon

sodiation/desodiation were performed. The cells under the selected voltages were disassembled for ex situ XRD tests (Fig. S12), and the corresponding contour plot in the range of 30° to 36° can observe the phase change more clearly (Fig. 3g) [47–49]. The diffraction peaks of the monoclinic Fe_7S_8 and cubic FeS_2 can be obviously observed in the pristine electrode. After discharging to 0.75 V, the diffraction peak of the FeS_2 disappears and the Na_xFeS_2 phase gradually forms, which can be attributed to the intercalation of Na^+ into the FeS_2 [21, 22]. After further discharging to 0.48 V, the diffraction peaks of Fe_7S_8 and FeS_2 disappear completely. Subsequently, diffraction peaks of Na_2S and Fe can be observed in the fully discharged state (0.05 V), suggesting that $\text{Fe}_7\text{S}_8/\text{FeS}_2/\text{NCNT}$ experiences the Na^+ insertion and phase transition upon discharge [18]. During the charging process, the characteristic peaks, corresponding to the Na_2S and Fe, gradually weaken, combined with the appearance of Na_xFeS_2 , suggesting the deintercalation of Na^+ . Finally, the formation of FeS_2 and Fe_7S_8 suggests the reverse phase transition, highlighting its superior electrochemical reversibility [23]. Figure 3h typically illustrates the working mechanism of $\text{Fe}_7\text{S}_8/\text{FeS}_2/\text{NCNT}$ electrode during sodiation/desodiation process. It undergoes a two-step reaction mechanism upon sodium storage: the Na^+ intercalation and phase transformation during the discharge process; the reverse conversion reaction and Na^+ extraction during the charging process [23].

In addition to improving electrochemical performance from material synthesis perspective, it has been found that electrolytes can greatly influence the structural evolution and electrochemical performance of iron sulfide-based electrodes in SIBs. Figure 4 compares the cycling performance and rate capacity of $\text{Fe}_7\text{S}_8/\text{FeS}_2/\text{NCNT}$ electrodes in ester/ether-based electrolytes. Figure 4a evaluates the cycling stability of the $\text{Fe}_7\text{S}_8/\text{FeS}_2/\text{NCNT}$ electrode in those two electrolytes. Particularly, an impressive capacity of 466.7 mAh g^{-1} is maintained after 1,000 cycles at 5.0 A g^{-1} in the ether-based electrolytes, demonstrating its robust cycle life. For comparison, negligible capacity can be detected of $\text{Fe}_7\text{S}_8/\text{FeS}_2/\text{NCNT}$ electrode after 500 cycles in the ester-based electrolyte. In addition, the initial Coulombic efficiency (ICE) of 73.4% can be obtained in the ether-based electrolyte, which is much higher than that in the ester-based electrolyte (60.5%). This could be attributed to the high electrochemical reversibility of electrode in ether-based electrolyte. Besides, a superior CE can be detected

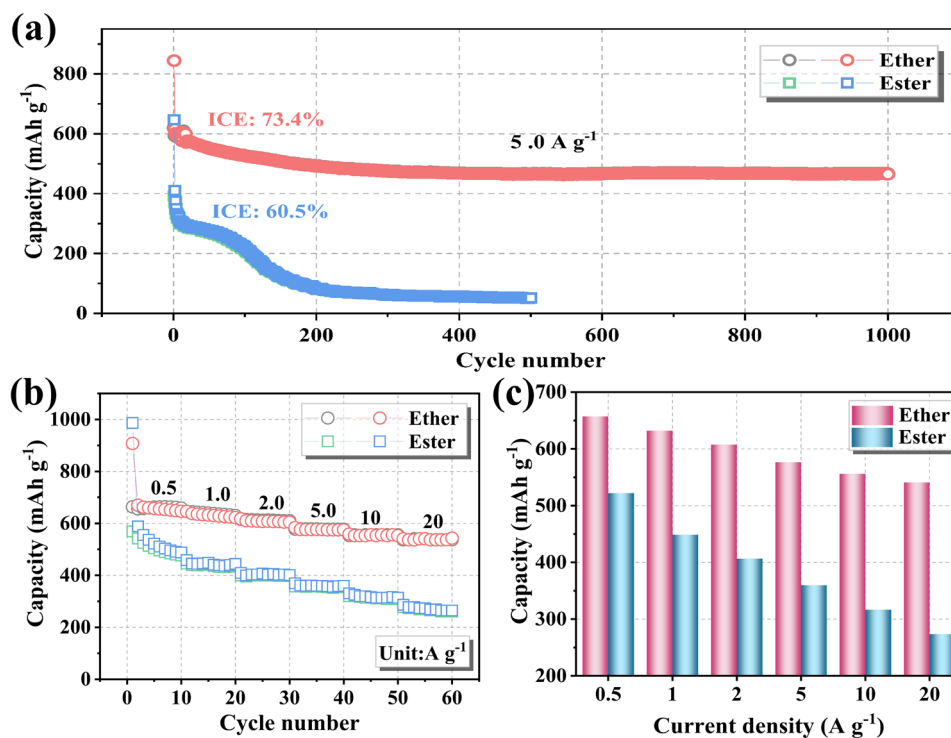


Fig. 4 (a) Cycling performance and (b) rate performance comparison of $\text{Fe}_7\text{S}_8/\text{FeS}_2/\text{NCNT}$ electrode in ester/ether-based electrolytes; (c) corresponding specific capacity at various current densities in two different electrolytes

in ether-based electrolyte ($\sim 100\%$) than that in ester-based electrolyte (Fig. S13). In general, the excellent CE in the ether-based electrolyte could be attributed to the uniform and stable SEI generated on the electrode surfaces, which can efficiently prevent further consumption of electrolyte and thus improve electrochemical reversibility [30, 50].

Figure 4b-c further compares the rate capacities of $\text{Fe}_7\text{S}_8/\text{FeS}_2/\text{NCNT}$ electrodes in those two electrolytes. Even at 20 A g^{-1} , a high capacity of 536.5 mAh g^{-1} can be maintained in the ether-based electrolyte, and the capacity retention rate is about 81.7% for the reversible capacity at 0.5 A g^{-1} . However, only 52.4% of the capacity can be retained in the ester-based electrolyte. Figure S14 shows discharge–charge profiles of the $\text{Fe}_7\text{S}_8/\text{FeS}_2/\text{NCNT}$ electrode at different current densities in the ether-based electrolyte. The charge/discharge curves at different current densities are almost consistent and show longer charge potential plateaus, contributing to the outstanding rate capability and high specific capacity [51]. Besides, the superior electrochemical sodium storage performance of as-prepared $\text{Fe}_7\text{S}_8/\text{FeS}_2/\text{NCNT}$ can be also confirmed through the comparison with other related studies (Table S1), from where the target

$\text{Fe}_7\text{S}_8/\text{FeS}_2/\text{NCNT}$ shows excellent sodium storage, mainly resulting from the heterostructure design and combination with NCNT [16].

Although the ether-based electrolyte has been identified as a key factor in achieving the excellent electrochemical properties of TMS-based anodes for SIBs, the origin of the positive effect of ether-based electrolyte on TMS-based anodes remains poorly understood. To prove the positive effect of ether-based electrolyte on electrode integrity, SEM investigations were performed on the electrode after cycling. The SEM image of the pristine $\text{Fe}_7\text{S}_8/\text{FeS}_2/\text{NCNT}$ electrode shows the typical tubular structure, which indicates that the electrode fabrication process plays little effect on its morphology (Fig. 5a). After cycling, the microstructure of $\text{Fe}_7\text{S}_8/\text{FeS}_2/\text{NCNT}$ electrode is well maintained in the ether-based electrolyte, and the tubular morphology is still clearly visible, which highlights the robust integrity of the electrode in ether-based electrolyte (Fig. 5b). In contrast, obvious agglomeration on the electrode after cycling can be detected in ester-based electrolyte (Fig. 5c), indicating the large volume change upon cycling [50, 52]. Furthermore, the cross-sectional SEM images show that the thickness of

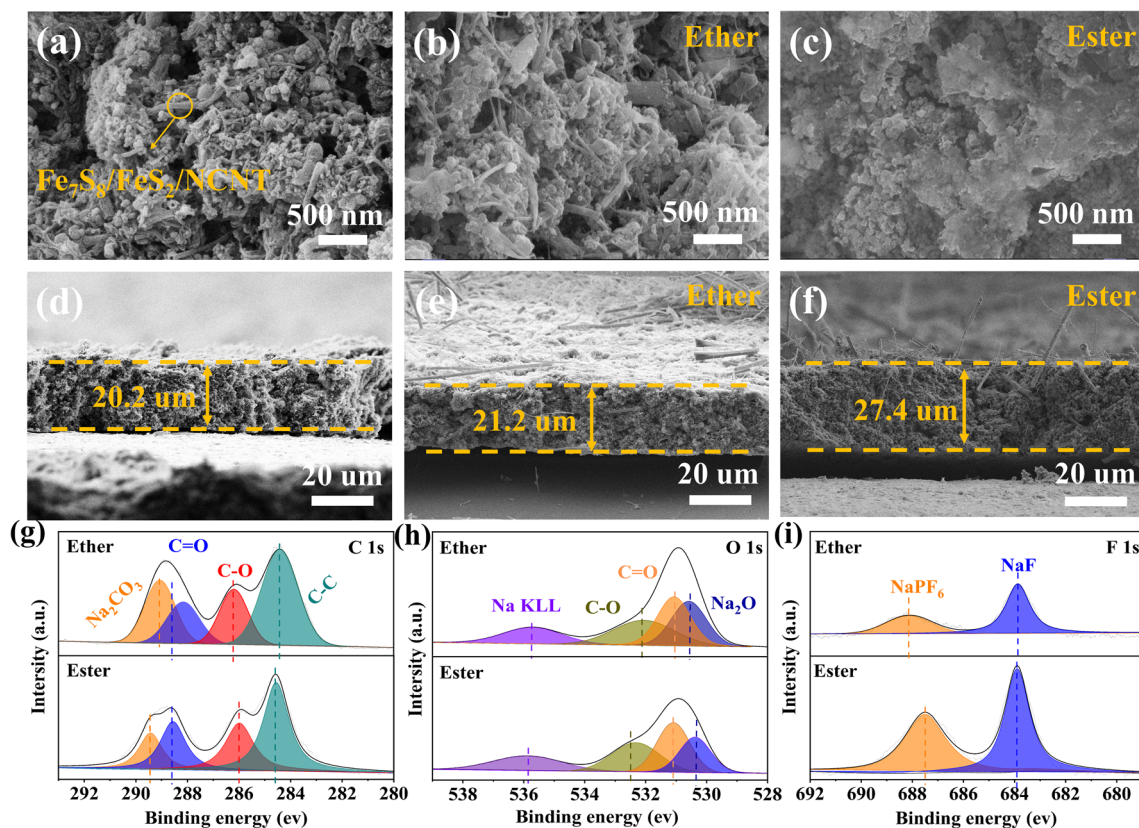


Fig. 5 (a) SEM and (d) cross-sectional images of the pristine Fe₇S₈/FeS₂/NCNT electrode. After 100 cycles at 1.0 Ag⁻¹, the SEM and cross-sectional images in (b, e) ether and (c, f) ester-based electrolytes. Comparison of the XPS spectra of Fe₇S₈/FeS₂/NCNT electrode after 100 cycles in these two electrolytes: (g) C 1s, (h) O 1s, (i) F 1s

the pristine electrode and the thickness of the electrodes after cycling in ether-based and ester-based electrolytes are 20.2, 21.2, and 27.4 μm, respectively (Fig. 5d, e, f). The swelling ratio of the electrode in ester-based electrolyte is 35.6%, which is much higher than that in the ether-based electrolyte (5%), demonstrating that the structural change of the electrode is alleviated after coupling with ether-based electrolyte [52, 53].

It's well known that ether-based electrode can induce a dense and robust SEI film on electrode surface, thereby providing fast charge transfer at the interface, reducing irreversible reactions, and maintaining the electrode integrity [52, 53]. To observe the chemical components on the SEI layer formed in different electrolytes, XPS measurements were carried out on the electrode after cycling. In the C 1s spectra of the electrodes, the characteristic peaks corresponding to C=O, Na₂CO₃, C-O, and C-C can be found in both two electrolytes (Fig. 5g). Meanwhile, the O 1s spectra exhibit four fitting peaks corresponding to the Na₂O, C-O, C=O,

and polyester, respectively (Fig. 5h) [13, 27]. Clearly, the Na₂CO₃ and Na₂O signals account for a larger proportion in the ether-derived SEI layer, which means that the ether-derived SEI film is mainly composed of inorganic components. It has been reported that relatively high inorganic components in the SEI layer are more likely to form a robust and dense SEI film, contributing to interfacial kinetics and charge transfer [52, 53]. Regarding the F 1s spectra, signals ascribed to the NaF and NaPF₆ species can be detected in both electrolytes (Fig. 5i) [53]. While the peak areas of NaF and NaPF₆ in ether-derived SEI layer are much smaller than those of ester-derived SEI layer, indicating a large amount of electrolyte is consumed during the SEI generation in the ester-based electrolytes. This further proves that the electrode is more stable when cycled in the ether-based electrolyte [50, 54].

Next, CV, electrochemical impedance spectroscopy (EIS), and galvanostatic intermittent titration (GITT) were conducted to evaluate Na⁺ kinetics differences of Fe₇S₈/

FeS₂/NCNT electrode in the ester/ether-based electrolytes. First of all, the electrochemical behaviors of the Fe₇S₈/FeS₂/NCNT in the ether-based electrolyte (0.01–3 V) have been investigated through the CV measurements (Fig. 6a), which match well with that in the ester-based electrolyte. Moreover, compared with the cathodic/anodic peaks in the ester-based electrolyte, the redox peaks become much sharper in the ether-based electrolyte, indicating an improved redox activity. Additionally, the CV curves of Fe₇S₈/FeS₂/NCNT electrode at various scan rates in the ether-based electrolyte display significant left shifting of the cathodic peak and right shifting of the anodic

peak, demonstrating its faintish electrochemical polarization [50]. Meanwhile, the charge/discharge profiles of the Fe₇S₈/FeS₂/NCNT electrode exhibit increased discharge platform and reduced charge platform, which indicate lower electrochemical polarization in the ether-based electrolyte, leading to the superior redox reversibility (Fig. S15) [54, 55]. Furthermore, the calculated b values for the Fe₇S₈/FeS₂/NCNT in ether-based electrolyte are higher than those in ester-based electrolyte, which indicate that the electrode coupled with ether-based electrolyte features rapid interfacial kinetics and larger capacitive contribution for charge storage (Fig. 6b) [30, 32]. To be more specific,

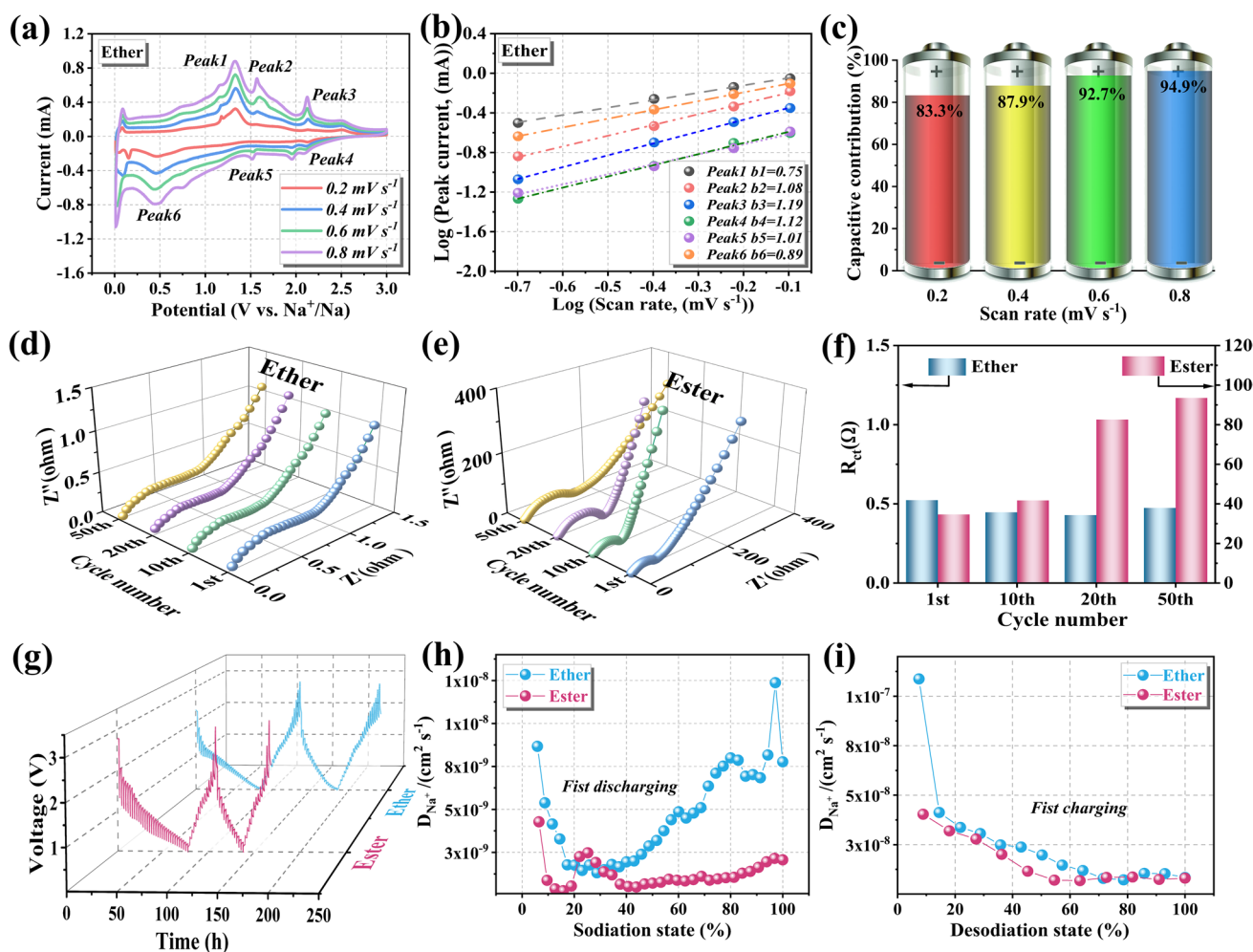


Fig. 6 (a) The CV curves at different scan rates (from 0.2 to 0.8 mV s^{-1}), (b) linear relationship of peak currents Log (i) versus scan rate Log (v), (c) capacity contributions of capacitive and diffusion-controlled behaviors at different scan rates of the Fe₇S₈/FeS₂/NCNT electrode in the ether-based electrolyte. Nyquist plots of the Fe₇S₈/FeS₂/NCNT electrode at 1st, 10th, 20th, and 50th cycles at 1 A g^{-1} from 0.01 to 10^7 Hz in (d) ether-based and (e) ester-based electrolytes, and (f) corresponding R_{ct} values. (g) GITT curves of the Fe₇S₈/FeS₂/NCNT electrode during the first two cycles as a function of time in the voltage of 0.01 to 3 V in different electrolytes. The diffusion coefficients of sodium ion during the initial (h) discharge and (i) charge process in different electrolytes

the capacitive contribution at various scan rates can be verified by the following equation [56, 57]:

$$i = k_1 v + k_2 v^{1/2} \quad (2)$$

where $k_1 v$ represents the contribution from capacitive behaviors, while $k_2 v^{1/2}$ corresponds to the contribution from diffusion [56, 57]. As can be seen from Fig. 6c, the capacitive contributions in ether-based electrolyte gradually increase from 83.3% to 94.9% as the scan rate increases, which are much larger than those in the ester-based electrolyte (Fig. S16). Specifically, after data collection and fitting, as displayed by the shaded areas in Figs. S17 and S18. Generally, good electrochemical kinetics at high current densities can be obtained from high capacitive contribution, which is beneficial for the rate capability and cycling stability [57].

The EIS comparison of the $\text{Fe}_7\text{S}_8/\text{FeS}_2/\text{NCNT}$ electrode at 1st, 10th, 20th, and 50th cycles at 0.1 A g^{-1} in ether/ester-based electrolytes have been illustrated in Fig. 6d, e. The semicircle and straight line observed at the high-frequency and low-frequency regions represent the charge transfer resistance (R_{ct}) and Warburg factor, respectively [58]. As shown in Fig. 6f, the lower R_{ct} values in ether-based electrolyte indicate rapid charge transfer and stable interface [56]. For the ester-based electrolyte, the R_{ct} value increases significantly from 34.6 (1st cycle) to 93.5 Ω (50th cycle), which can be attributed to the formation of a thick and unstable SEI layer caused by the ester-based electrolyte and then slow down the interfacial kinetics [53].

Besides, GITT investigation was carried out to compare the Na^+ diffusion coefficient in different electrolytes. In general, the diffusion coefficient of sodium ion can be evaluated based on the following equation [59, 60]:

$$D_{\text{Na}^+} = \frac{4}{\pi \tau} \left(\frac{m_b V_m}{M_b S} \right)^2 \left(\frac{\Delta E_s}{\Delta E_\tau} \right)^2, \tau \ll L^2/D_{\text{Na}^+} \quad (3)$$

where M_b , m_b , V_m , S and τ represent the molecular weight, the mass loading of active material, the molar volume of the electrode material, the surface area of the electrode, and the applied current, respectively, while ΔE_s and ΔE_τ correspond to the steady-state voltage change after the discharge pulse and the voltage variation during the discharge pulse [59, 60]. Figure 6g–i depicts the GITT curves and the calculated diffusion coefficients of the $\text{Fe}_7\text{S}_8/\text{FeS}_2/\text{NCNT}$ electrode in ether-based and ester-based electrolytes (mainly ranging from 10^{-11} to $10^{-7} \text{ cm}^2 \text{ s}^{-1}$). Specifically, the average diffusion coefficients of Na^+ upon the first discharge and charge in the ether-based electrolyte are 4.71×10^{-9} and $2.66 \times 10^{-8} \text{ cm}^2 \text{ s}^{-1}$, respectively. As a comparison, the

ester-based electrolyte exhibits relatively low diffusion coefficients, obtaining 1.24×10^{-9} and $1.62 \times 10^{-8} \text{ cm}^2 \text{ s}^{-1}$ during the first discharge and charge, respectively. Similarly, the variation trend of Na^+ diffusion coefficients in the second cycle of the two electrolyte is similar to that in the first cycle (Fig. S19), suggesting good electrochemical reversibility and stable ion transport channels [59, 60].

4 Conclusions

In summary, the rationally designed $\text{Fe}_7\text{S}_8/\text{FeS}_2/\text{NCNT}$ heterostructures have been successfully fabricated via an in situ pyrolysis and sulfidation strategy. The as-prepared $\text{Fe}_7\text{S}_8/\text{FeS}_2/\text{NCNT}$ features $\text{Fe}_7\text{S}_8/\text{FeS}_2$ heterostructure embedded in the hollow carbon nanotubes. The unique nano-architecture provides abundant lattice defects, superior electronic conductivity, and sufficient buffer space to maintain the integrity of the electrode during cycling. Consequently, the $\text{Fe}_7\text{S}_8/\text{FeS}_2/\text{NCNT}$ electrode delivered high sodium storage capacity, rapid ionic diffusion kinetics, and remarkable electrochemical reversibility. In particular, the $\text{Fe}_7\text{S}_8/\text{FeS}_2/\text{NCNT}$ electrode exhibits even more stable long-term cycling performance (466.7 mAh g^{-1} after 1,000 cycles at 5 A g^{-1}) and rate capability (536.5 mAh g^{-1} at 20 A g^{-1}) in ether-based electrolyte, which endows the battery with rapid ion diffusion kinetics, low charge-transfer resistance, high capacitive contribution to charge storage and robust SEI layer. The advanced $\text{Fe}_7\text{S}_8/\text{FeS}_2/\text{NCNT}$ heterostructure design and in-depth investigation on the origin of the superior electrochemical performances in ether-based electrolyte have paved the way for the development of TMS-based electrodes in sodium storage system.

Acknowledgements T.Y. Wang would like to acknowledge the support by the National Natural Science Foundation of China (G. No. 22102141).

Funding Open access funding provided by Shanghai Jiao Tong University.

Open Access This article is licensed under a Creative Commons Attribution 4.0 International License, which permits use, sharing, adaptation, distribution and reproduction in any medium or format, as long as you give appropriate credit to the original author(s) and the source, provide a link to the Creative Commons licence, and indicate if changes were made. The images or other third party material in this article are included in the article's Creative Commons licence, unless indicated otherwise in a credit line to the material. If material is not included in the article's Creative Commons licence and your intended use is not permitted by statutory regulation or exceeds the permitted use, you will need to obtain

permission directly from the copyright holder. To view a copy of this licence, visit <http://creativecommons.org/licenses/by/4.0/>.

Supplementary Information The online version contains supplementary material available at <https://doi.org/10.1007/s40820-023-01082-w>.

References

1. D. Su, Y. Pei, L. Liu, Z. Liu, J. Liu et al., Wire-in-wire TiO₂/C nanofibers free-standing anodes for Li-ion and K-ion batteries with long cycling stability and high capacity. *Nano-Micro Lett.* **13**(1), 107 (2021). <https://doi.org/10.1007/s40820-021-00632-4>
2. X. Chi, M. Li, J. Di, P. Bai, L. Song et al., A highly stable and flexible zeolite electrolyte solid-state Li-air battery. *Nature* **592**(7855), 551–557 (2021). <https://doi.org/10.1038/s41586-021-03410-9>
3. Y. Li, Q. Zhou, S. Weng, F. Ding, X. Qi et al., Interfacial engineering to achieve an energy density of over 200 wh kg⁻¹ in sodium batteries. *Nat. Energy* **7**(1), 2076 (2022). <https://doi.org/10.1038/s41560-022-01033-6>
4. T.P. Nguyen, A.D. Easley, N. Kang, S. Khan, S.M. Lim et al., Polypeptide organic radical batteries. *Nature* **593**(7857), 61–66 (2021). <https://doi.org/10.1038/s41586-021-03399-1>
5. G. Zhu, X. Tian, H.C. Tai, Y.Y. Li, J. Li et al., Rechargeable Na/Cl₂ and Li/Cl₂ batteries. *Nature* **596**(7873), 525–530 (2021). <https://doi.org/10.1038/s41586-021-03757-z>
6. P. Chen, T. Wang, F. Tang, G. Chen, C. Wang, Elaborate interface design of CoS₂/Fe₇S₈/NG heterojunctions modified on a polypropylene separator for efficient lithium-sulfur batteries. *Chem. Eng. J.* **446**(1), 136990 (2022). <https://doi.org/10.1016/j.cej.2022.136990>
7. J. Xie, Y.C. Lu, A retrospective on lithium-ion batteries. *Nat. Commun.* **11**(1), 2499 (2020). <https://doi.org/10.1038/s41467-020-16259-9>
8. H. Li, Y. Ma, H. Zhang, T. Diemant, R.J. Behm et al., Metal-organic framework derived Fe₇S₈ nanoparticles embedded in heteroatom-doped carbon with lithium and sodium storage capability. *Small Methods* **4**(12), 2000637 (2020). <https://doi.org/10.1002/smt.202000637>
9. J. Peng, W. Zhang, Q. Liu, J. Wang, S. Chou et al., Prussian blue analogues for sodium-ion batteries: Past, present, and future. *Adv. Mater.* **34**(15), e2108384 (2022). <https://doi.org/10.1002/adma.202108384>
10. L. Yue, Y. Qi, Y. Niu, S. Bao, M. Xu, Low-barrier, dendrite-free, and stable Na plating/stripping enabled by gradient sodiophilic carbon skeleton. *Adv. Energy Mater.* **11**(48), 2102497 (2021). <https://doi.org/10.1002/aenm.202102497>
11. B. Yan, L. Lin, C. Sun, L. Gao, H. Tao et al., Rational design of double-shelled Cu₂MoS₄@N-doped carbon hierarchical nanoboxes toward fast and stable sodium-ion batteries. *J. Mater. Chem. A* **10**(33), 17185–17198 (2022). <https://doi.org/10.1039/d2ta05119b>
12. J. Yang, J. Li, T. Wang, P.H.L. Notten, H. Ma et al., Novel hybrid of amorphous Sb/N-doped layered carbon for high-performance sodium-ion batteries. *Chem. Eng. J.* **407**(1), 127169 (2021). <https://doi.org/10.1016/j.cej.2020.127169>
13. J. Li, S. Tang, Z. Li, C. Wang, J. Li et al., Crosslinking nanoarchitectonics of nitrogen-doped carbon/MoS₂ nanosheets/Ti₃C₂T_x Mxene hybrids for highly reversible sodium storage. *Chemsuschem* **14**(23), 5293–5303 (2021). <https://doi.org/10.1002/cssc.202101902>
14. J. Li, J. Li, Z. Ding, X. Zhang, Y. Li et al., In-situ encapsulation of Ni₃S₂ nanoparticles into N-doped interconnected carbon networks for efficient lithium storage. *Chem. Eng. J.* **378**(1), 122108 (2019). <https://doi.org/10.1016/j.cej.2019.122108>
15. A. Jin, M.-J. Kim, K.-S. Lee, S.-H. Yu, Y.-E. Sung, Spindle-like Fe₇S₈/N-doped carbon nanohybrids for high-performance sodium ion battery anodes. *Nano Res.* **12**(3), 695–700 (2019). <https://doi.org/10.1007/s12274-019-2278-y>
16. X. Chen, D. Wang, J. Chen, Facile synthesis of uniform yolk-shell structured FeS@mesoporous carbon spheres for high-performance sodium-ion batteries. *New J. Chem.* **43**(26), 10291–10296 (2019). <https://doi.org/10.1039/c9nj01510h>
17. J. Zhang, Z. Meng, D. Yang, K. Song, L. Mi et al., Enhanced interfacial compatibility of FeS@N, S-C anode with ester-based electrolyte enables stable sodium-ion full cells. *J. Energy Chem.* **68**(1), 27–34 (2022). <https://doi.org/10.1016/j.jechem.2021.11.033>
18. C. Zhang, D. Wei, F. Wang, G. Zhang, J. Duan et al., Highly active Fe₇S₈ encapsulated in N-doped hollow carbon nanofibers for high-rate sodium-ion batteries. *J. Energy Chem.* **53**(1), 26–35 (2021). <https://doi.org/10.1016/j.jechem.2020.05.011>
19. S. Kandula, B. Sik Youn, J. Cho, H.-K. Lim, J. Gon Son, FeS₂@N-C nanorattles encapsulated in N/S dual-doped graphene/carbon nanotube network composites for high performance and high rate capability anodes of sodium-ion batteries. *Chem. Eng. J.* **439**(1), 135678 (2022). <https://doi.org/10.1016/j.cej.2022.135678>
20. Q. Li, Y. Liu, S. Wei, L. Xu, X. Wu et al., Box-like FeS@nitrogen-sulfur dual-doped carbon as high-performance anode materials for lithium ion and sodium ion batteries. *J. Electroanalytical Chem.* **903**(1), 115848 (2021). <https://doi.org/10.1016/j.jelechem.2021.115848>
21. H. Wu, N. Xu, Z. Jiang, A. Zheng, Q. Shi et al., Space and interface confinement effect of necklace-box structural FeS₂/WS₂ carbon nanofibers to enhance Na⁺ storage performance and electrochemical kinetics. *Chem. Eng. J.* **427**(1), 131002 (2022). <https://doi.org/10.1016/j.cej.2021.131002>
22. S. Wang, P. Ning, S. Huang, W. Wang, S. Fei et al., Multifunctional NiS₂/FeS₂/N-doped carbon nanorods derived from metal-organic frameworks with fast reaction kinetics for high performance overall water splitting and lithium-ion batteries. *J. Power Sources* **436**(1), 226857 (2019). <https://doi.org/10.1016/j.jpowsour.2019.226857>

23. Q. Peng, Y. Lu, S. Qi, M. Liang, D. Xu et al., Pomegranate-inspired nitrogen-doped carbon-coated bimetallic sulfides as a high-performance anode of sodium-ion batteries and their structural evolution analysis. *ACS Appl. Energy Mater.* **5**(3), 3199–3207 (2022). <https://doi.org/10.1021/acsaem.1c03810>
24. J. Li, S. Tang, Z. Li, C. Wang, L. Pan, Boosting the lithium storage performance by synergistically coupling ultrafine heazlewoodite nanoparticle with N, S co-doped carbon. *J. Colloid Interface Sci.* **604**(1), 368–377 (2021). <https://doi.org/10.1016/j.jcis.2021.07.031>
25. J. Yang, Z. Liu, X. Sheng, J. Li, T. Wang et al., Tin nanoparticle in situ decorated on nitrogen-deficient carbon nitride with excellent sodium storage performance. *J. Colloid Interface Sci.* **624**(1), 40–50 (2022). <https://doi.org/10.1016/j.jcis.2022.05.090>
26. Y. Li, F. Wu, Y. Li, M. Liu, X. Feng et al., Ether-based electrolytes for sodium ion batteries. *Chem. Soc. Rev.* **51**(1), 4484–4536 (2022). <https://doi.org/10.1039/d1cs00948f>
27. J. Li, Z. Ding, J. Li, C. Wang, L. Pan et al., Synergistic coupling of NiS_{10,3} nanoparticle with S-doped reduced graphene oxide for enhanced lithium and sodium storage. *Chem. Eng. J.* **407**(1), 127199 (2021). <https://doi.org/10.1016/j.cej.2020.127199>
28. Y. Liu, L. Zhang, D. Liu, W. Hu, X. Yan et al., Turbostratic carbon-localised FeS₂ nanocrystals as anodes for high-performance sodium-ion batteries. *Nanoscale* **11**(33), 15497–15507 (2019). <https://doi.org/10.1039/c9nr05594k>
29. S. Chen, S. Huang, J. Hu, S. Fan, Y. Shang et al., Boosting sodium storage of Fe_{1-x}S/MoS₂ composite via heterointerface engineering. *Nano Micro Lett.* **11**(1), 80 (2019). <https://doi.org/10.1007/s40820-019-0311-z>
30. M. Zhou, H. Tao, K. Wang, S. Cheng, K. Jiang, Nano-embedded microstructured FeS₂@C as a high capacity and cycling-stable Na-storage anode in an optimized ether-based electrolyte. *J. Mater. Chem. A* **6**(47), 24425–24432 (2018). <https://doi.org/10.1039/c8ta07571a>
31. L. Song, H. Fan, X. Fan, H. Gong, T. Wang et al., A simultaneous phosphorization and carbonization strategy to synthesize a defective Co₂P/doped-CNTs composite for bifunctional oxygen electrocatalysis. *Chem. Eng. J.* **435**(1), 134612 (2022). <https://doi.org/10.1016/j.cej.2022.134612>
32. F. Yang, S. Wang, J. Guan, L. Shao, X. Shi et al., Hierarchical MoS₂-NiS nanosheet-based nanotubes@N-doped carbon coupled with ether-based electrolytes towards high-performance Na-ion batteries. *J. Mater. Chem. A* **9**(47), 27072–27083 (2021). <https://doi.org/10.1039/d1ta08719c>
33. H. Li, Y. He, Y. Dai, Y. Ren, T. Gao et al., Bimetallic SnS₂/NiS₂@S-rGO nanocomposite with hierarchical flower-like architecture for superior high rate and ultra-stable half/full sodium-ion batteries. *Chem. Eng. J.* **427**(1), 131784 (2022). <https://doi.org/10.1016/j.cej.2021.131784>
34. B. Chen, J. Ding, X. Bai, H. Zhang, M. Liang et al., Engineering pocket-like graphene-shell encapsulated FeS₂: inhibiting polysulfides shuttle effect in potassium-ion batteries. *Adv. Funct. Mater.* **32**(14), 2109899 (2021). <https://doi.org/10.1002/adfm.202109899>
35. Z. Ma, Y. Liu, J. Gautam, W. Liu, A.N. Chishti et al., Embedding cobalt atom clusters in CNT-wired MoS₂ tube-in-tube nanostructures with enhanced sulfur immobilization and catalyzation for Li-S batteries. *Small* **17**(39), e2102710 (2021). <https://doi.org/10.1002/smll.202102710>
36. X. Wu, H. Zhao, J. Xu, Z. Zhang, W. Sheng et al., Facile synthesis of MOFs derived Fe₇S₈/C composites for high capacity and long-life rechargeable lithium/sodium batteries. *Appl. Surf. Sci.* **492**(1), 504–512 (2019). <https://doi.org/10.1016/j.apsusc.2019.06.217>
37. L. Shao, J. Hong, S. Wang, F. Wu, F. Yang et al., Urchin-like FeS₂ hierarchitectures wrapped with N-doped multi-wall carbon nanotubes@rGO as high-rate anode for sodium ion batteries. *J. Power Sources* **491**(1), 229627 (2021). <https://doi.org/10.1016/j.jpowsour.2021.229627>
38. X. Liu, P. Mei, Y. Dou, R. Luo, Y. Yamauchi et al., Hetero-architecturing a novel three-dimensional hierarchical MoO₂/MoS₂/carbon electrode material for high-energy and long-life lithium storage. *J. Mater. Chem. A* **9**(22), 13001–13007 (2021). <https://doi.org/10.1039/d1ta01706c>
39. Z. Hu, H. Cui, Y. Zhu, G. Lei, Z. Li, Holey reduced graphene oxide nanosheets wrapped hollow FeS₂@C spheres as a high-performance anode material for sodium-ion batteries. *J. Power Sources* **536**(1), 231438 (2022). <https://doi.org/10.1016/j.jpowsour.2022.231438>
40. Q. Zhang, Y. Zeng, C. Ling, L. Wang, Z. Wang et al., Boosting fast sodium ion storage by synergistic effect of heterointerface engineering and nitrogen doping porous carbon nanofibers. *Small* **18**(13), e2107514 (2022). <https://doi.org/10.1002/smll.202107514>
41. Y. Xu, J. Li, J. Sun, L. Duan, J. Xu et al., Implantation of Fe₇S₈ nanocrystals into hollow carbon nanospheres for efficient potassium storage. *J. Colloid Interface Sci.* **615**(1), 840–848 (2022). <https://doi.org/10.1016/j.jcis.2022.02.041>
42. Y. Huang, X. Hu, J. Li, J. Zhang, D. Cai et al., Rational construction of heterostructured core-shell Bi₂S₃@Co₉S₈ complex hollow particles toward high-performance Li- and Na-ion storage. *Energy Storage Mater.* **29**(1), 121–130 (2020). <https://doi.org/10.1016/j.ensm.2020.04.004>
43. Y. Zhou, M. Zhang, Q. Han, Y. Liu, Y. Wang et al., Hierarchical 1 T-MoS₂/Mo_x@NC microspheres as advanced anode materials for potassium/sodium-ion batteries. *Chem. Eng. J.* **428**(1), 131113 (2022). <https://doi.org/10.1016/j.cej.2021.131113>
44. X. Xie, X. Ma, Z. Yin, H. Tong, H. Jiang et al., Bimetallic heterojunction of CuSe/ZnSe@nitrogen-doped carbon with modified band structures for fast sodium-ion storage. *Chem.*



- Eng. J. **446**(1), 137366 (2022). <https://doi.org/10.1016/j.cej.2022.137366>
45. T. Ruan, B. Wang, Y. Yang, X. Zhang, R. Song et al., Interfacial and electronic modulation via localized sulfurization for boosting lithium storage kinetics. *Adv. Mater.* **32**(17), e2000151 (2020). <https://doi.org/10.1002/adma.202000151>
 46. Y. Rao, J. Wang, P. Liang, H. Zheng, M. Wu et al., Heterostructured WS_2/MoS_2 @carbon hollow microspheres anchored on graphene for high-performance Li/Na storage. *Chem. Eng. J.* **443**(1), 136080 (2022). <https://doi.org/10.1016/j.cej.2022.136080>
 47. C. Jiang, X. Meng, Y. Zheng, J. Yan, Z. Zhou et al., High-performance potassium-ion-based full battery enabled by an ionic-drill strategy. *CCS Chem.* **3**(1), 85–94 (2021). <https://doi.org/10.31635/ccschem.021.202000463>
 48. C. Jiang, Y. Fang, W. Zhang, X. Song, J. Lang et al., A multi-ion strategy towards rechargeable sodium-ion full batteries with high working voltage and rate capability. *Angew. Chem. Int. Ed.* **57**(50), 16370–16374 (2018). <https://doi.org/10.1002/anie.201810575>
 49. D. Yan, Y.V. Lim, G. Wang, Y. Shang, X.L. Li et al., Unlocking rapid and robust sodium storage performance of zinc-based sulfide via indium incorporation. *ACS Nano* **15**(5), 8507–8516 (2021). <https://doi.org/10.1021/acsnano.1c00131>
 50. W. Xiao, Q. Sun, J. Liu, B. Xiao, Y. Liu et al., Boosting the sodium storage behaviors of carbon materials in ether-based electrolyte through the artificial manipulation of microstructure. *Nano Energy* **66**(1), 104177 (2019). <https://doi.org/10.1016/j.nanoen.2019.104177>
 51. S.A. He, Z. Cui, Q. Liu, G. He, D.J.L. Brett et al., Enhancing the electrochemical performance of sodium-ion batteries by building optimized $NiS_2/NiSe_2$ heterostructures. *Small* **17**(45), e2104186 (2021). <https://doi.org/10.1002/smll.202104186>
 52. R. Dong, L. Zheng, Y. Bai, Q. Ni, Y. Li et al., Elucidating the mechanism of fast Na storage kinetics in ether electrolytes for hard carbon anodes. *Adv. Mater.* **33**(36), e2008810 (2021). <https://doi.org/10.1002/adma.202008810>
 53. C. Zhang, F. Wang, F. Han, H. Wu, F. Zhang et al., Improved electrochemical performance of sodium/potassium-ion batteries in ether-based electrolyte: cases study of $MoS_2@C$ and $Fe_7S_8@C$ anodes. *Adv. Mater. Interfaces* **7**(13), 200486 (2020). <https://doi.org/10.1002/admi.202000486>
 54. Z. Lv, T. Li, X. Hou, C. Wang, H. Zhang et al., Solvation structure and solid electrolyte interface engineering for excellent Na^+ storage performances of hard carbon with the ether-based electrolytes. *Chem. Eng. J.* **430**(1), 133143 (2022). <https://doi.org/10.1016/j.cej.2021.133143>
 55. H. Yuan, F. Ma, X. Wei, J.L. Lan, Y. Liu et al., Ionic-conducting and robust multilayered solid electrolyte interphases for greatly improved rate and cycling capabilities of sodium ion full cells. *Adv. Energy Mater.* **10**(37), 2001418 (2020). <https://doi.org/10.1002/aenm.202001418>
 56. H. Zheng, J. Wang, H. Li, S. Deng, Y. Zuo et al., Constructing a novel heterostructure of $NiSe_2/CoSe_2$ nanoparticles with boosted sodium storage properties for sodium-ion batteries. *J. Mater. Chem. A* **10**(30), 16268–16279 (2022). <https://doi.org/10.1039/d2ta04237a>
 57. Y. Xia, L. Que, F. Yu, L. Deng, Z. Liang et al., Tailoring nitrogen terminals on Mxene enables fast charging and stable cycling Na-ion batteries at low temperature. *Nano Micro. Lett.* **14**(1), 143 (2022). <https://doi.org/10.1007/s40820-022-00885-7>
 58. H. Wu, X. Chen, X. Zhang, Z. Jiang, Y. Dong et al., Multi-dimensional nanobox structural carbon nanofibers with dual confined effect for boosting storage performance and electrochemical kinetics of alkali metal ion batteries. *Chem. Eng. J.* **428**(1), 131207 (2022). <https://doi.org/10.1016/j.cej.2021.131207>
 59. C. Ma, Z. Xu, J. Jiang, Z. Ma, T. Olsen et al., Tailored nanoscale interface in a hierarchical carbon nanotube supported $MoS_2@MoO_2-C$ electrode toward high performance sodium ion storage. *J. Mater. Chem. A* **8**(21), 11011–11018 (2020). <https://doi.org/10.1039/d0ta03390a>
 60. Y. Wang, W. Kang, X. Pu, Y. Liang, B. Xu et al., Template-directed synthesis of $Co_2P/MoSe_2$ in a N-doped carbon hollow structure for efficient and stable sodium/potassium ion storage. *Nano Energy* **93**(1), 106897 (2022). <https://doi.org/10.1016/j.nanoen.2021.106897>